Materials Characterization 179 (2021) 111294

Contents lists available at ScienceDirect

Materials Characterization

journal homepage: www.elsevier.com/locate/matchar

Investigation on the corrosion behavior of single-phase and binary-phase Mg-Sc alloys: An experimental and first-principles study

Tian Xie [a], Pengyu Zhao [a], Yuyang Chen [a], Manyu Zhang [a], Yaowei Wang [b], Tao Ying [a,*], Hong Zhu [b,c], Xiaoqin Zeng [a,*]

[a] National Engineering Research Center of Light Alloy Net Forming, Shanghai Jiao Tong University, Shanghai 200240, China
[b] University of Michigan - Shanghai Jiao Tong University Joint Institute, Shanghai Jiao Tong University, Shanghai 200240, China
[c] The State Key Lab of Metal Matrix Composites, Shanghai Jiao Tong University, Shanghai 200240, China

ARTICLE INFO

Keywords:
Mg-Sc alloys
Microstructure
First-principles calculations
Corrosion behavior

ABSTRACT

Microstructural characteristics and corrosion behaviors of the single-phase and binary-phase Mg-*x*Sc (wt%, x = 5, and 15) were investigated. Both single and binary phases Mg-Sc alloys display typical peritectic microstructure, where Sc-depleted areas are surrounded by Sc-rich zones. The MgSc phases are prone to precipitate in Mg-rich zones of Mg-15Sc, which is beneficial to the enhancement of yield strength. To analyze the corrosion behavior, experimental and first-principles studies were conducted. The single-phase Mg-5Sc alloy shows the lowest weight loss rate with 0.6 mg/cm^2/day, which is one order of magnitude smaller than that of binary-phase Mg-15Sc alloy. The potential difference, the cathode H_2 evolution kinetics, and the surface layer containing Sc_2O_3 are believed to be the main reasons for the corrosion behavior difference of single-phase and binary-phase Mg-Sc alloys.

1. Introduction

Magnesium (Mg) alloys are promising materials in the application of the aerospace, automotive, and 3C (Computer, Communication, and Customer Electronic) industries due to their attractive properties, such as high specific strength, high thermal conductivity, electromagnetic compatibility, and easy recycling [1]. However, Mg is a quite active element, which has a high negative standard potential (~ −2.372 V/NHE), and serves as an anode to dissolve or sacrifice. In addition, the naturally formed oxide layer of Mg is usually porous and soluble. The corrosive medium, especially the chloride ion, can easily attack the Mg substrate, and this problem has become the greatest obstacle for broadening the applications [2–7].

The worldwide researchers have attempted to improve the corrosion performance of Mg alloys. Birbilis et al. [8] reported single-phase Mg-As alloys possessed high corrosion resistance, owing to the suppressed cathodic hydrogen evolution. Liu et al. [9] further investigated single-phase Mg alloys with microalloying additions of group 14 and 15 elements and revealed that Bi, Ge, Pb, Sb, and Sn are capable of improving corrosion-resistance as As. Deng et al. [10] prepared single-phase Mg-Ca alloys by Ca micro-alloying with a protective film, showed extremely low corrosion rates. Herein, designing single-phase Mg alloys is an effective approach to improve the corrosion resistance. Nevertheless, the mechanical property of single-phase material is usually limited due to the absence of precipitation strengthening. A practical way to balance corrosion and mechanical performance is to design binary/multiphase Mg alloys. For instance, Xu et al. [11] declared a multiphase Mg-Li based alloy exhibiting high strength and corrosion resistance. Boby et al. [12] reported multiphase AZ91 alloys with addition of Sn and Y, possessing both excellent corrosion and mechanical performance. It is worth noting that binary/multiphase materials are susceptible to micro-galvanic corrosion, which may reduce the corrosion-resistant performance. In general, the abovementioned designing routes as single-phase and binary/multiphase Mg alloys should be considered according to the actual application requirement case by case.

Among the various alloying elements, rare earth (RE) elements are proved to be effective in enhancing the corrosion resistance of Mg alloy [12–15]. RE elements can not only improve the protection of the surface layer by forming RE oxide [16], but also lower the overpotential of hydrogen evolution [14]. Compared with other RE elements, scandium (Sc) yields a greater grain size refinement effect, possesses a high solubility in Mg (> 25 wt%), and the ability of cathodic-kinetics suppression

* Corresponding authors.
E-mail addresses: yingtao85@sjtu.edu.cn (T. Ying), xqzeng@sjtu.edu.cn (X. Zeng).

https://doi.org/10.1016/j.matchar.2021.111294
Received 20 May 2021; Received in revised form 28 June 2021; Accepted 30 June 2021
Available online 6 July 2021

[17]. Zhang et al. [18] reported the microstructure and corrosion behavior of single-phase Mg-Sc alloys with tiny Sc concentration, and the refined microstructure and the formation of protective corrosion products film were believed to be the reasons for the enhancement of anti-corrosion property. Thus, Sc is believed to be a promising candidate for designing high corrosion-resistant Mg alloy [14].

Therefore, in this study, single-phase and binary-phase Mg-Sc alloys are designed. The corrosion behavior of Mg-Sc based alloys is investigated and compared with commercial AZ91D alloy and high purity Mg. The underlying corrosion mechanism is discussed with the help of first-principles calculations.

2. Materials and methods

2.1. Materials

The alloy ingots with a nominal composition of Mg-5Sc and Mg-15Sc were prepared by conventional melting in an electric resistance furnace. High pure Mg (HP Mg, > 99.95 wt%) and Mg-30Sc (wt%) intermediate alloy were melted under a mixed atmosphere of CO_2 and SF_6 (melting and refining temperature: 730 °C). Then the melt was poured into a pre-heated steel mold. The chemical composition of these alloys was analyzed via inductively coupled plasma-atomic emission spectrometry (ICP-AES, X series II, Thermofisher Scientific, US), and the results are listed in Table 1. The commercial AZ91D alloy was used as a counterpart.

2.2. Microstructure characterization

The phase identification of all Mg alloys was conducted via X-ray diffraction (XRD, Philips, PW1700, the Netherlands) with a Cu Kα1 radiation of λ = 1.5406 Å at an accelerated voltage of 40 kV and 30 mA. The microstructures were observed by optical microscope (OM, Zeiss Axio Observer A1) and field-emission scanning electron microscopy (SEM, Philips XL-30FEG, the Netherlands) equipped with energy dispersive spectrometry (EDS). The cross-sectional morphology and structure of the corrosion product was characterized using transmission electron microscopy (TEM, Tecnai G2 F30), with the aid of selected-area electron diffraction (SAED) technique. The detailed description of the preparation of cross-sectional TEM specimens can be found elsewhere [19].

Dimension Icon & FastScan Bio scanning Kelvin probe force microscopy (SKPFM) was used to determine the potential difference between anode and cathode. The SKPFM measurements were operating in the tapping mode using a two-pass technique. The height data was recorded during the first pass, then the probe tip lifted and scanned following the height profile with the potential data recorded in the second pass. The tip to sample distance was kept constantly at 100 nm. Temperature and humidity levels were around 23 ± 2 °C and 60 ± 6% respectively during measurements.

X-ray photoelectron spectroscopy (XPS, ESCALAB250, Thermo VG) measurements were performed on the corroded Mg-Sc alloy to analyze the composition of the corrosion product. The XPSPEAK software (version 4.1) was used for peak fitting of the XPS data via referencing to a database (National Institute of Standards and Technology of US). The binding energy scale was corrected with the C 1 s peak at 284.6 eV as the reference.

2.3. Corrosion tests

The corrosion rate tests performed in this work includes H_2 collection and weight loss immersion. As for H_2 collection, the specimen was suspended with a nylon string in the 3.5 wt% NaCl solution for 48 h under an inverted glass funnel, and an acid burette was used to collect the H_2 gas [2]. In the weight loss measurements, the specimens were also immersed in 3.5 wt% NaCl solution. The corrosion products were removed by a mixed solution composed of a 200 g/L chromate acid solution, 10 g/L silver nitrate, and 20 g/L barium nitrate. The weight loss was determined by recording the weight before and after the immersion test. Each corrosion rate tests were repeated at least 3 times to ensure the reliability of experimental data.

The potentiodynamic polarization and electrochemical noise (EN) of Mg alloys were measured in 3.5 wt% NaCl solution at room temperature by using an electrochemical workstation (Autolab PGSTAT302N). During the potentiodynamic polarization test, a typical three-electrode cell was used, consisting of a platinum foil as the counter electrode, a saturated calomel electrode (SCE, saturated KCl) as the reference electrode and the Mg alloys as the working electrodes (WE). The specimens were polarized in the anodic and cathodic direction separately after 10 min of stabilization at the open circuit potential (OCP) with a scan rate of 0.33 $mV{\cdot}s^{-1}$. In the EN test, two identical specimens were applied as the working electrode and a SCE as the reference electrode, respectively. The electrochemical current noise was measured as the galvanic coupling current between two identical WE kept at the same potential. EN data was recorded at a data-sampling interval of 0.25 s after the immersion of the working electrodes in the solution. The total 691,200 data points were collected in 172,800 s.

2.4. Mechanical property

The room temperature tensile test was carried out on a Zwick/Roell Z100 testing machine with a cross-head speed of 0.5 mm/min. At least three parallel tests were replicated for each alloy to confirm the reliability of the results.

2.5. First-principles calculation

Density functional theory (DFT) calculations were performed on the Vienna Ab initio Simulation Package (VASP) [20] using the Perdew-Burke-Ernzerholf functional (PBE) [21] and the projector augmented wave (PAW) [22] method. The plane wave with a kinetic energy cutoff of 520 eV was settled, and Γ-centered k-meshes of 3 × 3 × 1 were used for the structural optimization and static calculations. K-mesh density in slab calculations was the same as that of bulk calculations. The electronic convergence criterion was set at 1×10^{-6} eV in the static calculation to get accurate energy and electrostatic potential. Eight layered p (3 × 3) slab was built to simulate HP Mg. As for Mg-5Sc, 2 Mg atoms were replaced on the subsurface of HP Mg slab model by Sc, respectively. To simulate the condition of Mg-15Sc and AZ91D alloys, MgSc and $Mg_{17}Al_{12}$ second phases models were set up. Nudged Elastic Band (NEB) method was used to calculate the reaction barriers [22]. During the NEB calculations, the structures set as the initial and final point in the reaction path were pre-relaxed until the forces on atoms were less than 10^{-4} eV/Å, while the images along reaction path were relaxed until the total forces on the atoms were less than 10^{-2} eV/Å [23,24].

Table 1
Chemical composition of investigated alloys (wt%).

Alloy	Sc	Al	Zn	Mn	Si	Fe	Cu	Mg
HP Mg	–	0.0195	0.0016	0.0038	0.0053	0.0034	0.0005	Bal.
Mg-5Sc	5.2410	0.0632	0.0125	0.0048	0.0733	0.0291	0.0050	Bal.
Mg-15Sc	15.0100	0.1280	0.0382	0.0044	0.1160	0.0459	0.0158	Bal.
AZ91D	–	9.2300	0.7300	0.2100	0.0290	0.0014	0.0018	Bal.

3. Results

3.1. Microstructural characterization

Fig. 1 shows the optical microstructure of Mg-Sc alloys. In general, the Mg-Sc alloys display the typical peritectic microstructural feature. Unlike other elements such as Al, Zn, Ca, etc., Sc tends to participate in the peritectic reaction with Mg instead of eutectic reaction, and the phase diagram of binary Mg-Sc alloy is given in reference [25, 26]. With the increasing of Sc content, the grains are distinctly refined due to the retarding of grain boundary migration, the detailed information about the effect of Sc on grain refinement can refer to the results in [27,28]. In addition, no second phases are observed in Mg-5Sc alloys, nevertheless, second phases begin to precipitate in α matrix when the Sc content further increases to 15%. This result is consistent with the XRD results shown in Fig. 1(c), only the peaks of Mg are observed in low Sc containing alloys, and the peaks corresponding to MgSc (β) phase [29,30] become discernable in Mg-15Sc alloy. Consequently, Mg-Sc alloys in this study can be divided into two types: single-phase alloy (Mg-5Sc) and binary-phase alloy (Mg-15Sc).

Fig. 2 shows the SEM microstructures of Mg-5Sc and Mg-15Sc. As for single-phase alloy, a characteristic peritectic microstructure is observed, where Sc rich zones are surrounded by α-Mg. Although most of Sc tends to present in a solid solution state, the distribution of Sc element is not homogenous, displaying a combination of Sc-rich central area and surrounding Sc-depleted region. In the case of binary-phase alloy, as shown in Fig. 2(d, e, f), the microstructure is generally analogous to that of Mg-5Sc alloy except for the precipitation of the second phase (as the arrow pointed) in Sc-rich zones.

To further identify the second phase in binary-phase Mg-15Sc alloy, TEM analysis result is shown in Fig. 3. The bright field images show the morphology of the second phase, and the corresponding SAED pattern is displayed in Fig. 3(b). The second phase piled up by rod-like precipitated particles is indeed MgSc phase according to the reference from the International Centre for Diffraction Data (ICDD) [29]. The diffraction spots of the $(0002)_\alpha$ and $(\bar{1}01)_\beta$ crystalline plane nearly coincide, and the $[111]_\beta$ direction of the CsCl-type (B2) MgSc phase is parallel to the $[11\bar{2}0]_\alpha$ direction of the hcp Mg matrix, i.e., $[11\bar{2}0]_\alpha // [111]_\beta$ [29].

3.2. Mechanical property

AZ91D is a widely used Mg alloy with a simultaneously high corrosion-resistant and mechanical properties. In this paper, we compared AZ91D and Mg-Sc alloys to evaluate the mechanical property of single-phase and binary-phase Mg-Sc alloys. As shown in Fig. 4, the yield strength (YS) and ultimate tensile strength (UTS) of Mg-Sc alloys both increase with Sc addition, whereas the enhancement in YS of single-phase alloys is less noticeable than that of binary-phase alloys. Compared with HP Mg, the YS almost increased one magnitude in Mg-15Sc alloy, which is even higher than that of AZ91D alloy. Apparently, the increase of YS and UTS in binary-phase alloy is attributed to the precipitation strengthening of MgSc second phase. Regarding the elongation part, the single-phase Mg-5Sc alloys show relatively high values than that of Mg-15Sc, causing by the probability reduction of

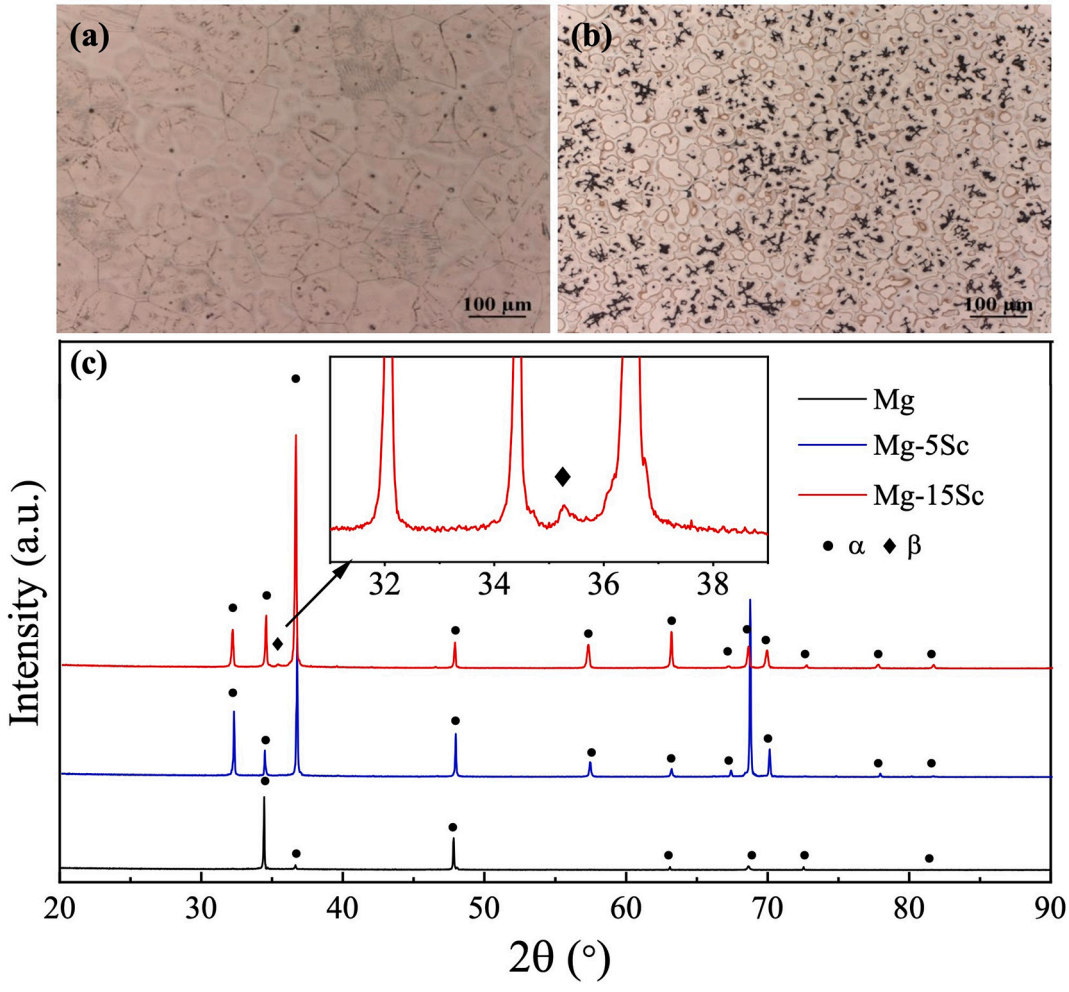

Fig. 1. Typical optical microstructure of Mg-Sc alloys: (a) Mg-5Sc; (b) Mg-15Sc; (c) XRD patterns of Mg and Mg-Sc alloys.

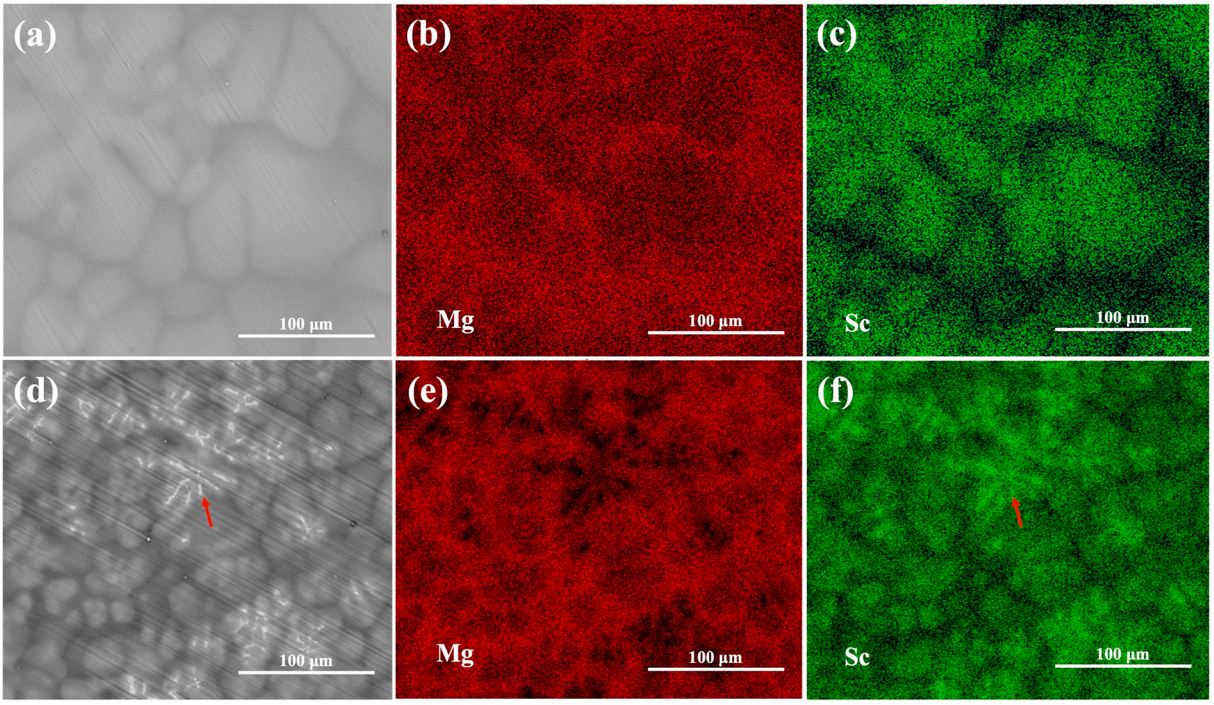

Fig. 2. Microstructure of Mg-5Sc: (a) Information collection scope of mapping, (b) distribution of element Mg, (c) distribution of element Sc; and Mg-15Sc: (d) Information collection scope of mapping, (e) distribution of element Mg, (f) distribution of element Sc.

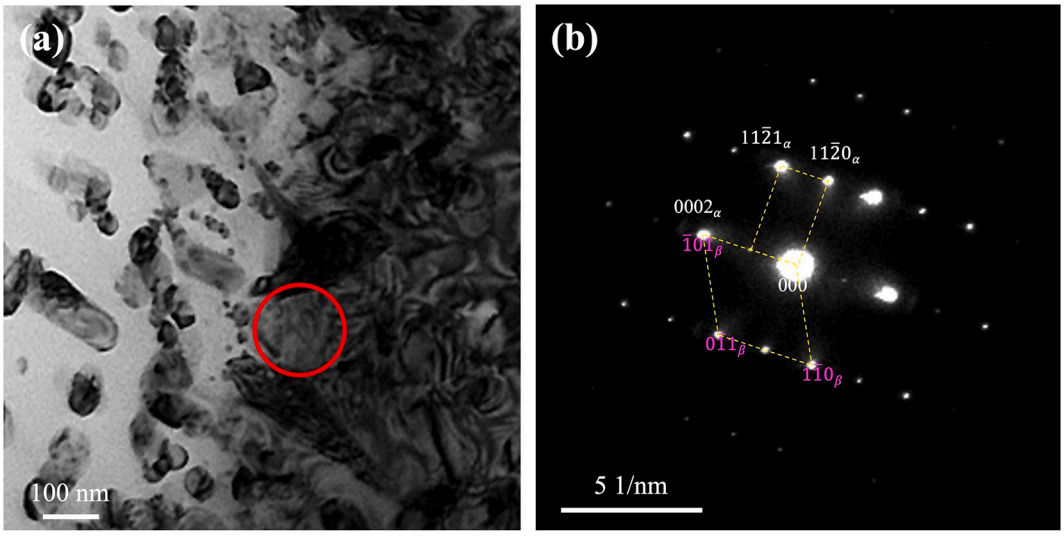

Fig. 3. (a) TEM bright field image of the second phase, (b) SAED pattern taken from (a), the electron beam direction is parallel to the $[11\bar{2}0]_\alpha$ direction of the hcp Mg matrix (α) and $[111]_\beta$ direction of the CsCl-type (B2) MgSc (β).

dislocations propagation and stress localization [31].

3.3. Corrosion results

3.3.1. The hydrogen evolution and weight loss measurement

To study the corrosion behavior of Mg-Sc alloys, H_2 evolution and weight loss tests were carried out and the results are illustrated in Fig. 5. Generally, the addition of Sc is favourable for anti-corrosion, especially in the single-phase Mg-Sc alloy, the corrosion rates of HP Mg nearly halved after Sc alloying [32]. However, with the further increase of Sc concentration, the corrosion rate starts to level up in binary-phase alloy because of the precipitation of MgSc second phase. It is worth noting that the corrosion rate of binary-phase alloy is still lower than that of AZ91D, indicating that scandium exerts a more positive influence on the improvement of corrosion resistance than aluminum. In sum, the ranking of corrosion rates can be summarized as follows: AZ91D > Mg-15Sc > HP Mg > Mg-5Sc. The results attest to the conjecture that single-phase alloy behaves better anti-corrosion property than binary-phase alloy.

3.3.2. Corrosion morphology characterization

The microscopic morphology after corrosion is given in Fig. 6(a, f, k). It is obvious that the surface layer of Mg-5Sc alloy is relatively uniform after 48 h immersion, while the surfaces are severely corroded with the presence of the second phase in AZ91D and Mg-15Sc alloys. Both second phases ($Mg_{17}Al_{12}$ and MgSc, as the arrow pointed in Fig. 6) are observed

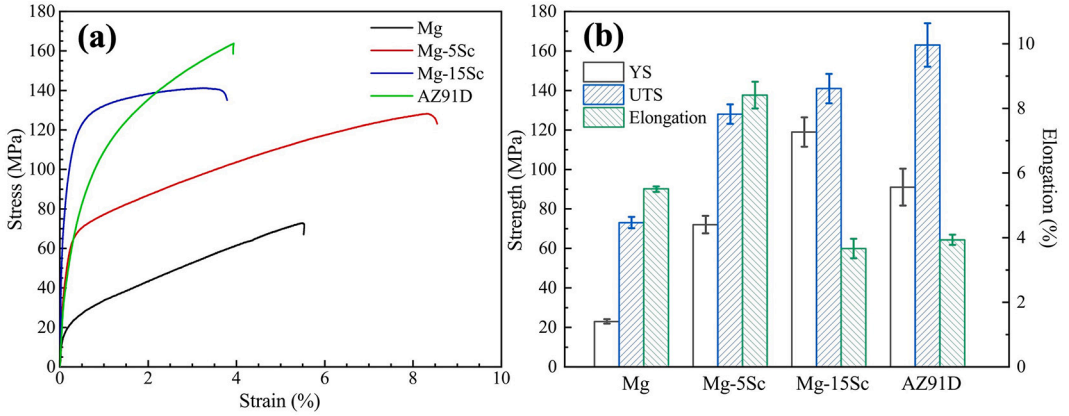

Fig. 4. (a) Typical engineering stress-strain curves of Mg, Mg-5Sc, Mg-15Sc and AZ91D alloys. (b) Variation of yield strength, ultimate tensile strength, and elongation of the investigated alloys at room temperature. The error bars correspond to the standard deviation based on at least three measurements performed on different specimens of each alloy.

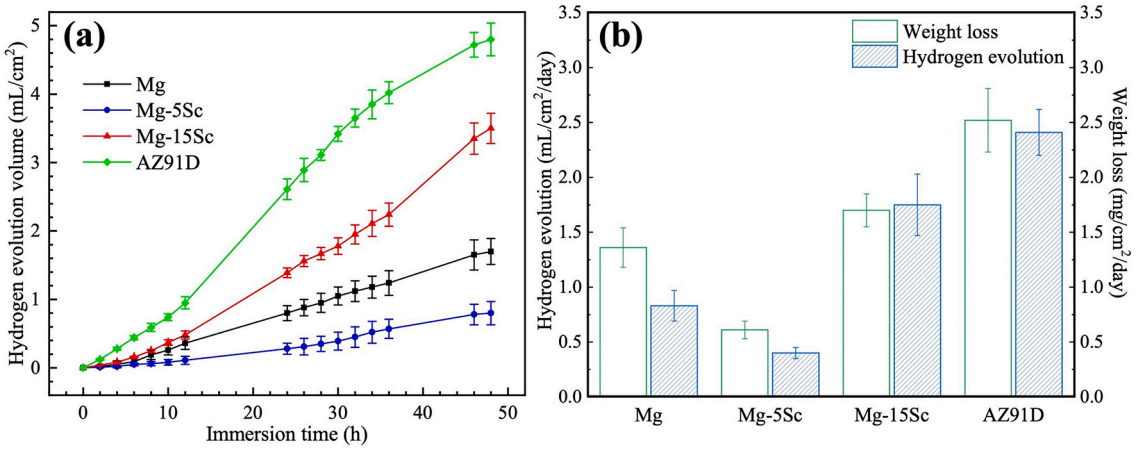

Fig. 5. (a) Hydrogen evolution of Mg, Mg-5Sc, Mg-15Sc, and AZ91D following 48 h immersion in 3.5 wt% NaCl. (b) Hydrogen evolution and weight loss results of Mg, Mg-5Sc, Mg-15Sc, and AZ91D following 48 h immersion in 3.5 wt% NaCl. The error bars correspond to the standard deviation based on at least three measurements performed on different specimens of each alloy.

close to the surface in AZ91D and Mg-15Sc alloys, and the nearby areas are corroded dramatically with little protection of the surface layer. The second phases tend to form micro-galvanic couples with Mg matrix, and the completeness of the surface could be excessively affected by the presence/absence of the second phase.

3.3.3. *Electrochemical measurements*

The short term (OCP for 10 min) and long term (OCP for 48 h) potentiodynamic polarization tests were carried out to evaluate the corrosion behaviors of Mg-Sc alloys, and the results are displayed in Fig. 7 and Table 2. As presented, single-phase alloy shows the lowest corrosion current density (i_{corr}) after 10 min OCP, followed by HP Mg, Mg-15Sc, and AZ91D. The ranking order is in good agreement with the hydrogen evolution and weight loss results. After 48 h immersion in 3.5 wt% NaCl solution, although the i_{corr} ranking does not change, an increase of i_{corr} and a noble shift of the corrosion potential (E_{corr}) are observed. It is interesting to note that a distinct breakdown potential can be observed in the anodic branch of Mg-5Sc alloy, either in short-term or long-term tests, suggesting the stability of the protective corrosion product layer in single-phase alloy [33]. However, no such breakdown signals are found in binary-phase Mg-15Sc alloy. Although its corrosion potential is the highest, in other words, the lowest corrosion tendency in all specimens, the actual protection of the corrosion product layer is relatively poor.

To further analyze the short-term and long-term behavior, electrochemical noise analysis is carried out and the results are shown in Fig. 8. As illustrated in Fig. 8(a), the electrochemical current noise was measured as the galvanic coupling current between two identical working electrodes kept at the same potential. The reciprocal of the noise resistance R_n is inversely proportional to the corrosion rate [19]. Thus, the real-time corrosion behavior is capable of recording without imposing disturbances. As the increase of immersion time, the corrosion rate is prone to accelerate with larger amplitude fluctuations, which indicates that the surface is undertaking the fierce competition process between pit initiation and passivation. During the 48 h immersion period, Mg-15Sc alloy keeps a high corrosion level throughout the whole process, as well as AZ91D. As for the HP Mg, the corrosion is slow in the initial stage but followed by a sharp accelerating after 6 h immersion. The reason is that the initial metastable pits grow into a larger stable pit, suddenly raise the value of the corrosion rate of HP Mg. The single-phase Mg-5Sc alloy maintains the continuously lowest corrosion rates during EN test, and this result agrees with that of potentiodynamic polarization tests.

4. Discussion

As the corrosion behavior of Mg alloys is sensitive to lots of intrinsic and environmental parameters, e.g. alloying, microstructure,

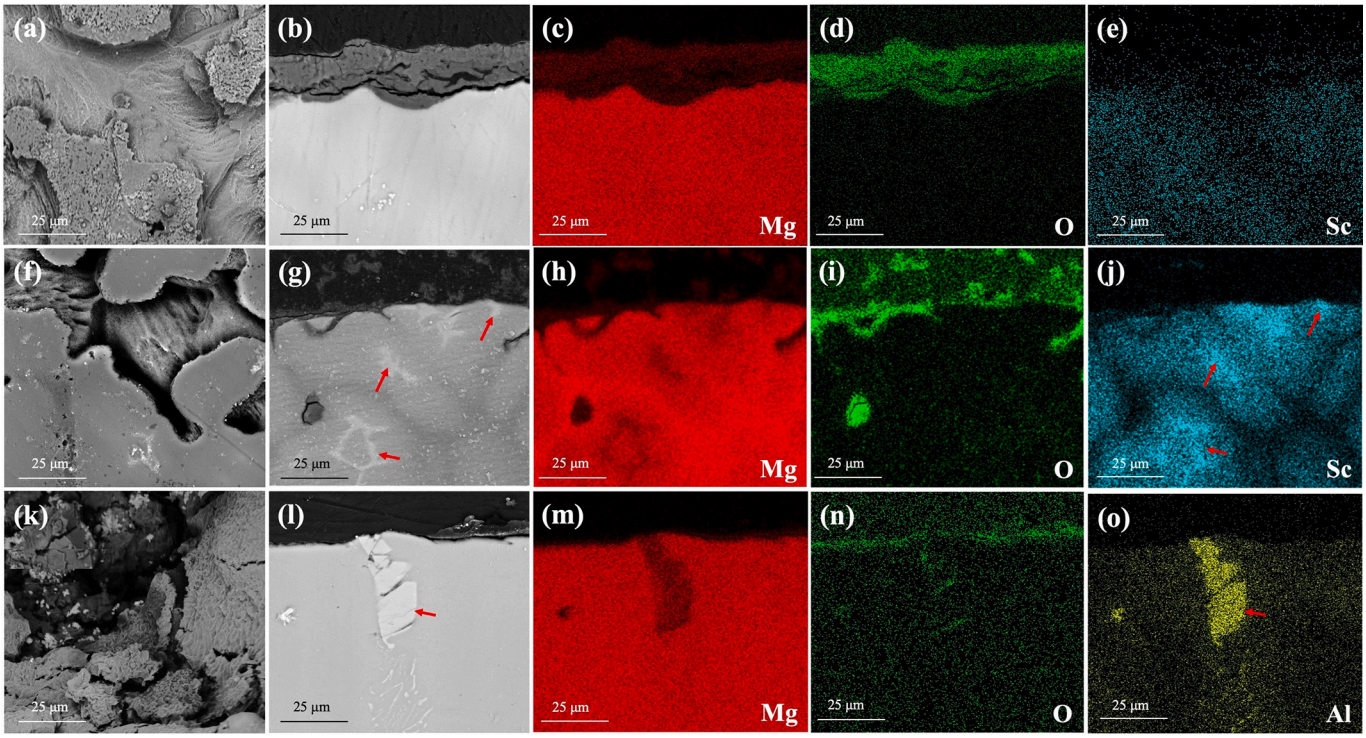

Fig. 6. Microscopic morphology with corrosion products removed and corrosion cross-section of (a, b) Mg-5Sc, (f, g) Mg-15Sc, (*k*,*l*) AZ91D and corresponding element distribution in the surface layer of: (c, d, e) Mg-5Sc; (h, i, j) Mg-15Sc; and, (m, n, o) AZ91D, after 48 h immersion in 3.5 wt% NaCl.

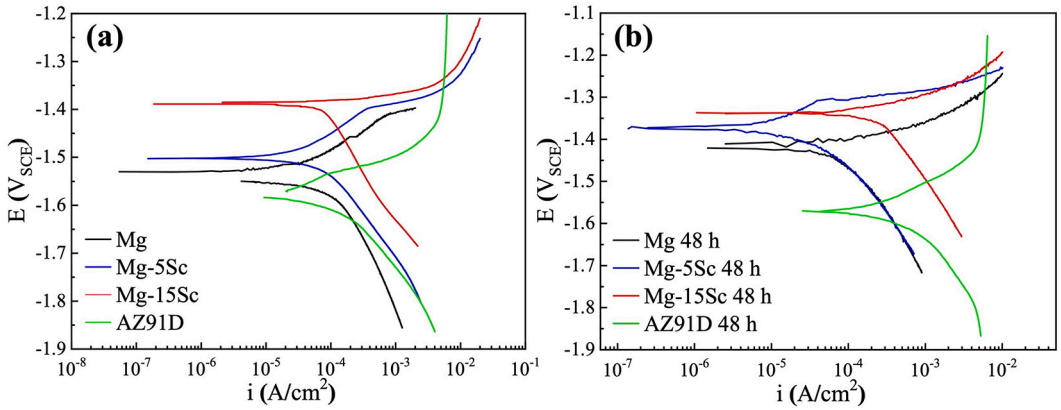

Fig. 7. The (a) potentiodynamic polarization curves (OCP for 10 min); (b) potentiodynamic polarization curves (OCP for 48 h) of Mg, Mg-5Sc, Mg-15Sc, and AZ91D alloys.

Table 2
Corrosion current density and potential of investigated alloys.

Alloy	i_{corr} (A/cm^2) 10 min	i_{corr} (A/cm^2) 48 h	E_{corr} (V_{SCE}) 10 min	E_{corr} (V_{SCE}) 48 h
HP Mg	4.81×10^{-5}	1.01×10^{-4}	−1.54	−1.41
Mg-5Sc	1.11×10^{-5}	1.61×10^{-5}	−1.51	−1.37
Mg-15Sc	8.31×10^{-5}	1.84×10^{-4}	−1.39	−1.33
AZ91D	9.63×10^{-5}	3.32×10^{-4}	−1.58	−1.56

temperature, pH, etc., the underlying corrosion mechanism is always hard to clarify. In the present work, first-principles calculations and experimental measurements were employed to understand the corrosion mechanism of single-phase and binary-phase Mg-Sc alloys, from the thermodynamic and kinetic perspectives of corrosion.

4.1. Thermodynamic driving force of corrosion

In solid physics, the intrinsic potential difference ($U_A - U_B$) between two different metals AB could be expressed as [34]:

$$U_A - U_B = \frac{(W_A - W_B)}{e} \quad (1)$$

W_A and W_B are the work functions of two metals. The work function is defined as the minimum work or energy required to get an electron out of metal [23,35]. When two phases contact, the intrinsic potential difference will promote the redistribution of charges, leading to galvanic corrosion [34]. The potential difference is often regarded as the thermodynamic driving force of galvanic corrosion [36]. The larger work function difference, the stronger corrosion tendency.

Fig. 9 shows the slab models and DFT calculated work function difference between HP Mg and Mg-5Sc solid solution, MgSc phase, and

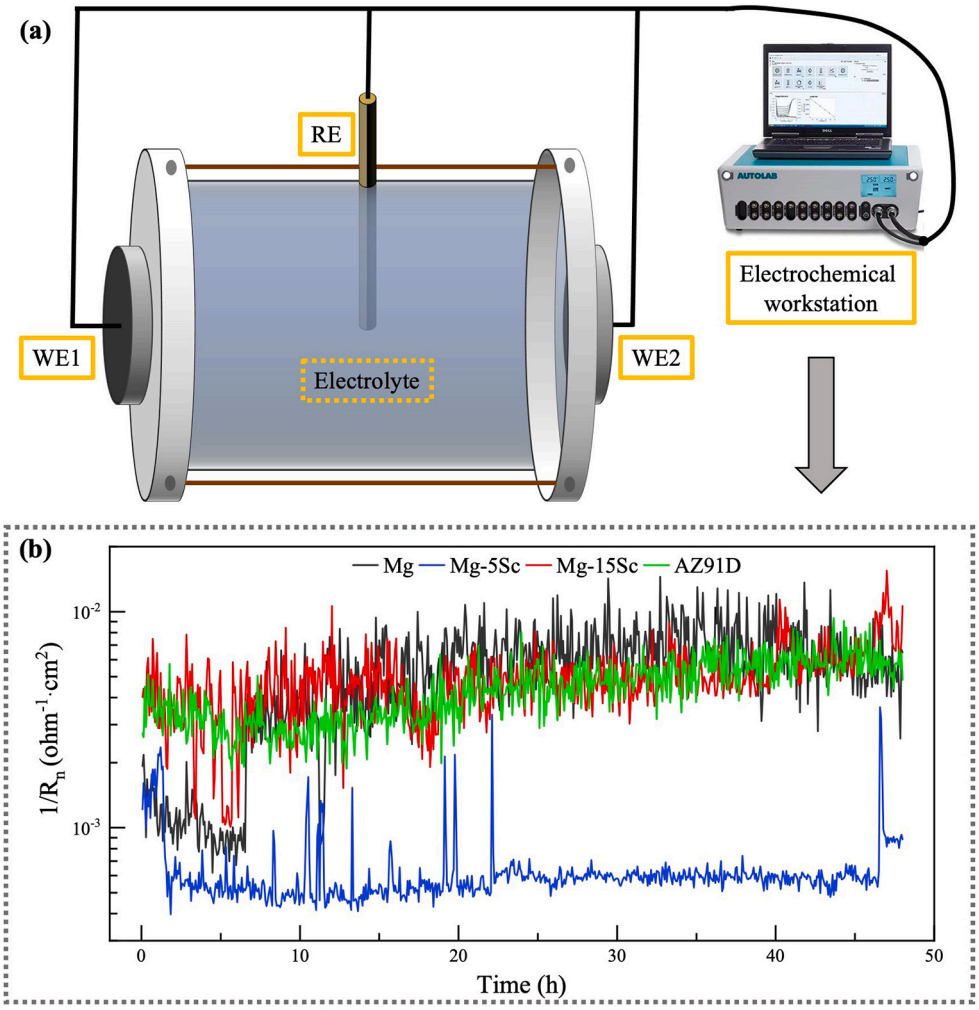

Fig. 8. (a) Schematic diagram of electrochemical noise test, with corresponding (b) results of Mg, Mg-5Sc, Mg-15Sc, and AZ91D alloys. WE and RE represent working electrode and reference electrode, respectively.

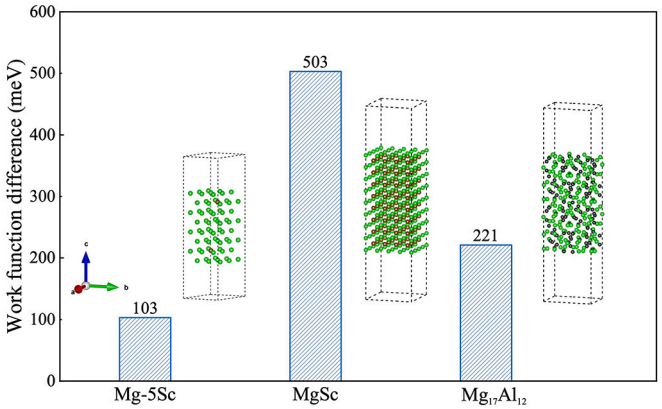

Fig. 9. DFT calculated work function difference between HP Mg and Mg-5Sc, MgSc, $Mg_{17}Al_{12}$. The atoms of the corresponding slab models are colored by type: Mg (green), Sc (brown), Al (black). (For interpretation of the references to colour in this figure legend, the reader is referred to the web version of this article.)

$Mg_{17}Al_{12}$ phase, the detailed set up process of the slab models could be found in Supplementary Material. Obviously, the work function differences between Mg-5Sc and HP Mg is the smallest, indicating the weakest corrosion driving force in single-phase alloying system. As for binary-phase Mg-15Sc and AZ91D alloys, the work function differences are much larger due to the presence of MgSc and $Mg_{17}Al_{12}$ second phases, and the corresponding thermodynamic driving forces are substantially stronger. It is noteworthy that the MgSc phase exerts an even higher corrosion tendency than $Mg_{17}Al_{12}$, though the corrosion rate of binary-phase Mg-Sc alloy is lower than that of AZ91D.

Excepting the DFT calculation, the SKPFM was applied to further analysis of the thermodynamics of the corrosion. As the results show in Fig. 10, the potential difference between Sc-rich regions and α-Mg is only about 30 mV, whereas the potential differences between α-Mg and second phases (MgSc and $Mg_{17}Al_{12}$) are as high as 390 mV and 190 mV, respectively. The potential difference in binary-phase Mg-15Sc alloy is indeed higher than that in AZ91D alloy. This experimental result is in accordance with the DFT calculation, which verifies the accuracy of the DFT result.

4.2. Corrosion products

In order to confirm the composition of corrosion product in Mg-Sc alloys, XPS analysis is adapted and the results are shown in Fig. 11. The peaks are corresponding to the reported binding energy [37–39]. In the case of Mg-Sc alloys, the immerged Sc peaks attest to the presence of Sc_2O_3 in the corrosion product of both single-phase and binary-phase Mg-Sc alloys. Meanwhile, the cross-section of Mg-5Sc crossion product is observed by TEM in Fig. 12, the surface layer is indeed composed of

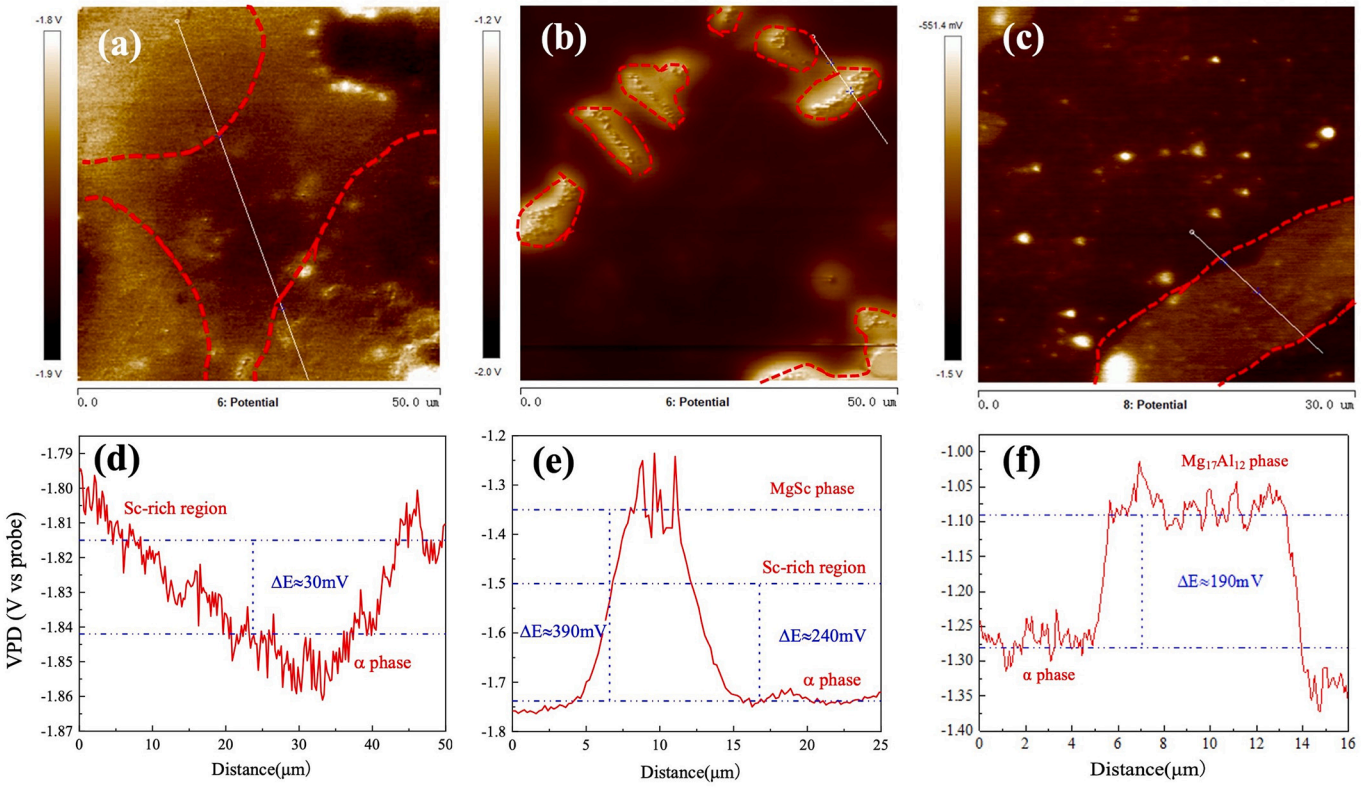

Fig. 10. Surface Volta potential map and line-profile analysis of: (a), (d) Mg-5Sc; (b), (e) Mg-15Sc; and (c), (f) AZ91D alloy.

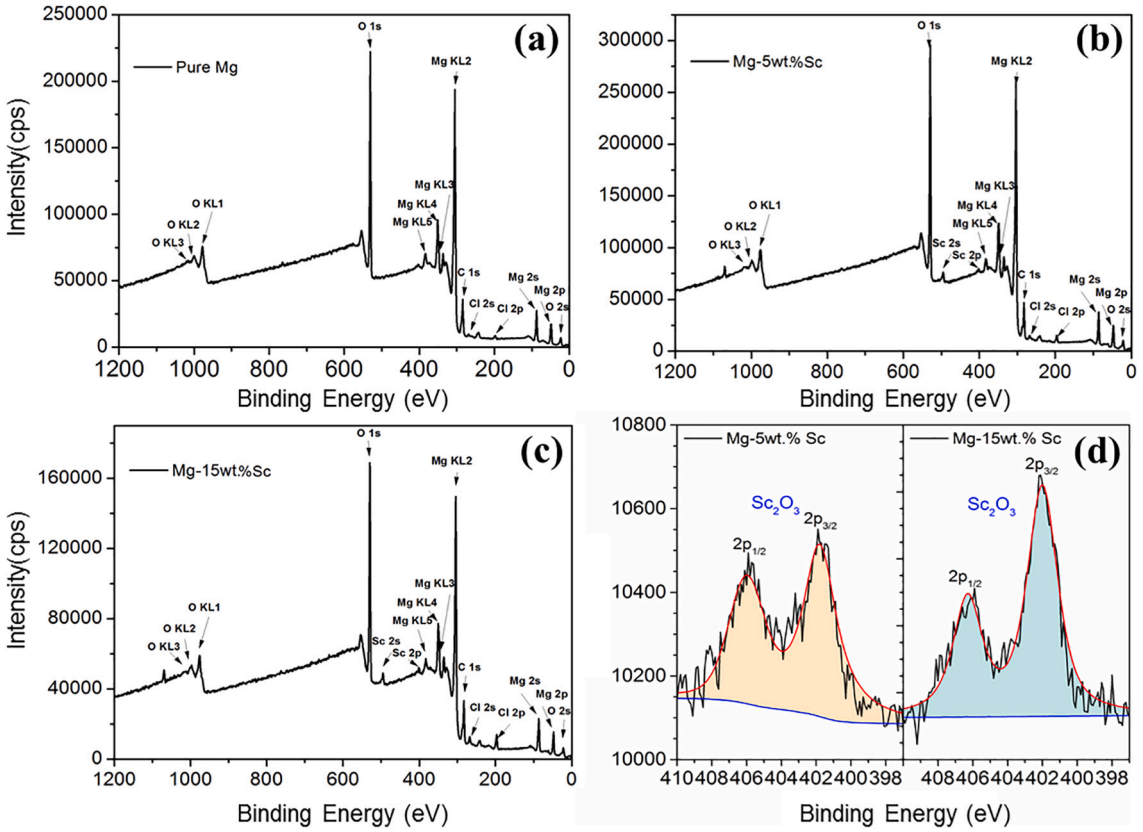

Fig. 11. XPS results of (a) HP Mg, (b) Mg-5Sc , and (c) Mg-15Sc alloys; And narrow spectra analysis of (d) the Sc 2p peaks of Mg-5Sc and Mg-15Sc alloys, unified proportionally referring to the Mg 2p peaks.

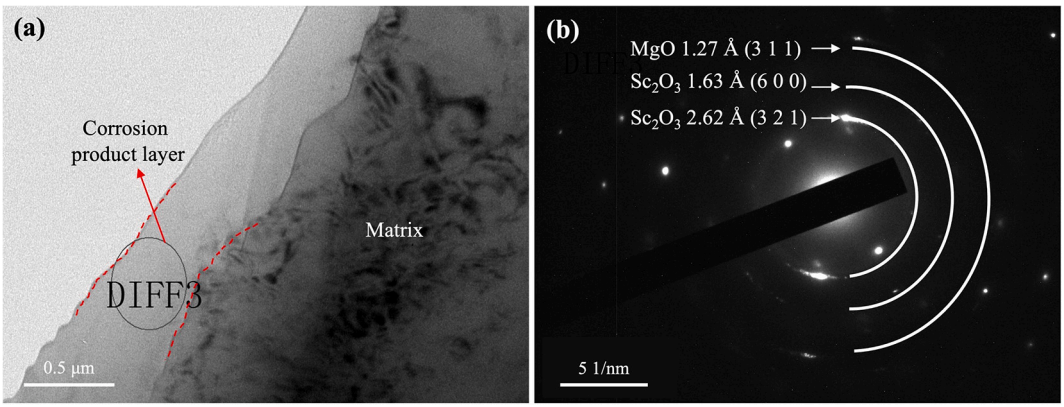

Fig. 12. (a) Dark-field TEM image and (b) corresponding SAED pattern of Mg-5Sc alloys.

Sc_2O_3 and MgO. As the Pilling-Bedworth (P-B) ratio of Sc_2O_3 (1.19) is much larger than that of MgO (0.81) [40], it is helpful to compensate for the volume mismatch between the Mg matrix and the corrosion production, so as to alter the structure and passivation ability of surface layer. In addition, the scandium oxide is insoluble in an aqueous solution, which would increase the stability of the surface layer. Therefore, the presence of Sc_2O_3 would be effective to improve the completeness and protectiveness of the surface layer.

To analyze the variation of Sc in the surface of single-phase and binary-phase Mg-Sc alloys, the Mg 2p peak is set as the reference, and the peaks of Sc elements are adjusted proportionally. The peak intensity ratio of Sc_2O_3, which is proportional to the volume fraction, do not show pronounced change in single-phase and binary-phase Mg-Sc alloys. Nevertheless, as shown in Fig. 6, the surface layer of single-phase Mg-5Sc is relatively completeness with the presence of Sc_2O_3, thereby preventing catastrophic failure of the surface layer.

4.3. Cathodic hydrogen evolution kinetics of corrosion

Therefore, with the presence of second phases in the surface layer, the corrosion behavior is strongly affected by the intrinsic corrosion behavior of the second phases. Herein, the first-principles calculation was used to study the cathodic kinetics. As Mg usually serves as an anode during the galvanic corrosion, and cathodic reaction accompanied with the H_2 evolution mainly takes place on second phases [23,24,41,42]. In the neutral or basic solution, the hydrogen evolution process could be separated into the following steps [24]: (1) the adsorbed water molecules ($*H_2O$) on the surface dissociate into hydrogen adatom (*H) and hydroxyl group (*OH) [43]; (2) the *H remains and the *OH consumes an electron and leaves as OH^- (the Volmer reaction); (3) two nearby *H diffuse and combine as H_2 gas (the Tafel reaction) [44]. The Heyrovsky reaction could be ignored because of the low H^+ concentration in the considered solution.

The surface energies of the different orientations of Mg-5Sc, MgSc, and $Mg_{17}Al_{12}$ were calculated, and Mg-5Sc(100), MgSc(100), and $Mg_{17}Al_{12}$(110) are the most stable surfaces, respectively. The adsorption energy of *H, *OH, H_2O, and H_2 molecule on the different sites of the most stable surfaces were calculated before NEB analyzation. The minimum energy path (MEP) of H_2O dissociation and H_2 recombination on the surface obtained by NEB method constrained geometry optimization

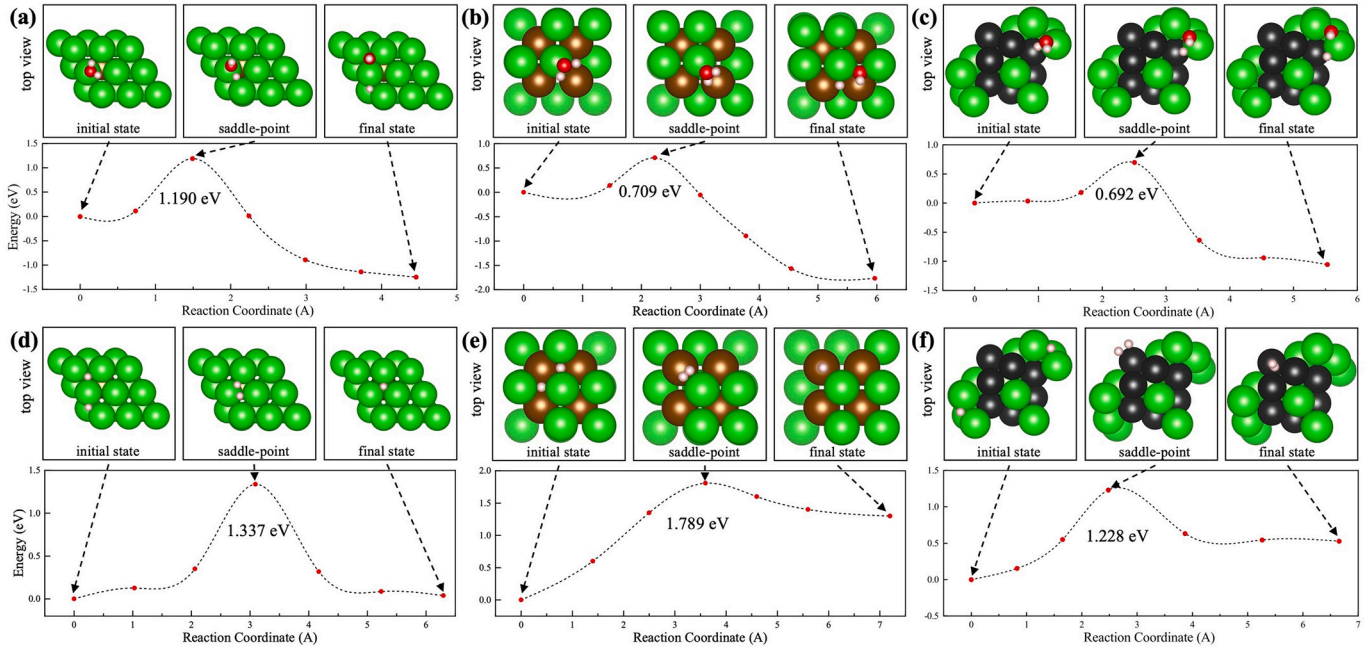

Fig. 13. Minimum energy path for H_2O molecule dissociation on: (a) Mg-5Sc, (b) MgSc, and (c) $Mg_{17}Al_{12}$ surface; and *H recombination on: (d) Mg-5Sc, (e) MgSc, and (f) $Mg_{17}Al_{12}$ surface. The atoms of the corresponding slab models are colored by type: Mg (green), Sc (brown), Al (black), O (red), H (white). (For interpretation of the references to colour in this figure legend, the reader is referred to the web version of this article.)

is shown in Fig. 13. The energy barriers of H_2O dissociation on Mg-5Sc, MgSc and $Mg_{17}Al_{12}$ surface are 1.190 eV, 0.709 eV, and 0.692 eV, respectively, which suggests that an H_2O molecule is most unfavored to decompose on the Mg-5Sc(100) surface.

Fig. 13 shows the MEP of H_2 combination in single-phase Mg-5Sc, binary-phase Mg-15Sc and AZ91D. The energy barrier on MgSc surface is the largest to be 1.789 eV, which is also the maximum energy barrier during the whole reaction path. This indicates the H_2 evolution is thermodynamically unfavored and the cathodic process could be suppressed with the presence of MgSc phase. Like the researchers have reported before, similar to As, Ge, and Cd, Sc could also reducing the cathodic kinetics in Mg alloys by tightly binding *H and prevent H_2 evolution [17,24], which meets well with our results. All in all, AZ91D has the lowest MEP of H_2O dissociation and H_2 recombination. With Sc addition to HP Mg, single-phase Mg-5Sc and binary-phase Mg-15Sc alloy could well suppress the cathodic hydrogen evolution dynamics.

4.4. Mechanism discussion

Fig. 14 illustrates the corrosion mechanism of the investigated alloys. Up to date, HP Mg has always been the benchmark of high corrosion-resistant magnesium because the addition of most alloying element is not able to improve the corrosion resistance [7]. However, what is striking herein is that the single-phase Mg-5Sc alloys display even better corrosion property than HP Mg in this study. In single-phase HP Mg and Mg-5Sc alloys, the corrosion driving force stays low at the beginning of corrosion, as the DFT calculation results revealed. However, typical corrosion products MgO/$Mg(OH)_2$ on HP Mg cannot provide reliable corrosion protection considering its porous structure. The addition of 5% Sc tends to change the structure of the surface layer and increase the pitting potential, which is beneficial to the improvement of corrosion resistance. What's more, the layer seems to own a strong passivation behavior due to the existence of Sc_2O_3 judging from the EN result.

In the case of binary-phase Mg-15Sc and AZ91D alloy, the precipitation of MgSc or $Mg_{17}Al_{12}$ would increase the micro-galvanic couples and enlarge the potential between the anodic/cathodic region, leading to the acceleration of the corrosion reaction and destruction of the completeness of the corrosion product layer. Compared with $Mg_{17}Al_{12}$ phase, although the potential difference is higher for MgSc phase, its ability to suppress H_2 evolution would be beneficial to corrosion resistance.

5. Conclusions

The microstructure characteristics and corrosion behaviors of the single-phase and binary-phase Mg-Sc alloys were investigated. Potentiodynamic polarization and electrochemical noise tests were conducted, combined with the analysis of surface layer and Volta potential difference. The underlying corrosion mechanism was unveiled assisted by the first-principles calculations. The main conclusions are listed as follows:

(1) Single-phase Mg-5Sc exhibits the best corrosion-resistant performance with a weight loss rate of 0.6 mg/cm^2/day, and the corrosion rates can be ranked as follows: Mg-5Sc < HP Mg < Mg-15Sc < AZ91D.

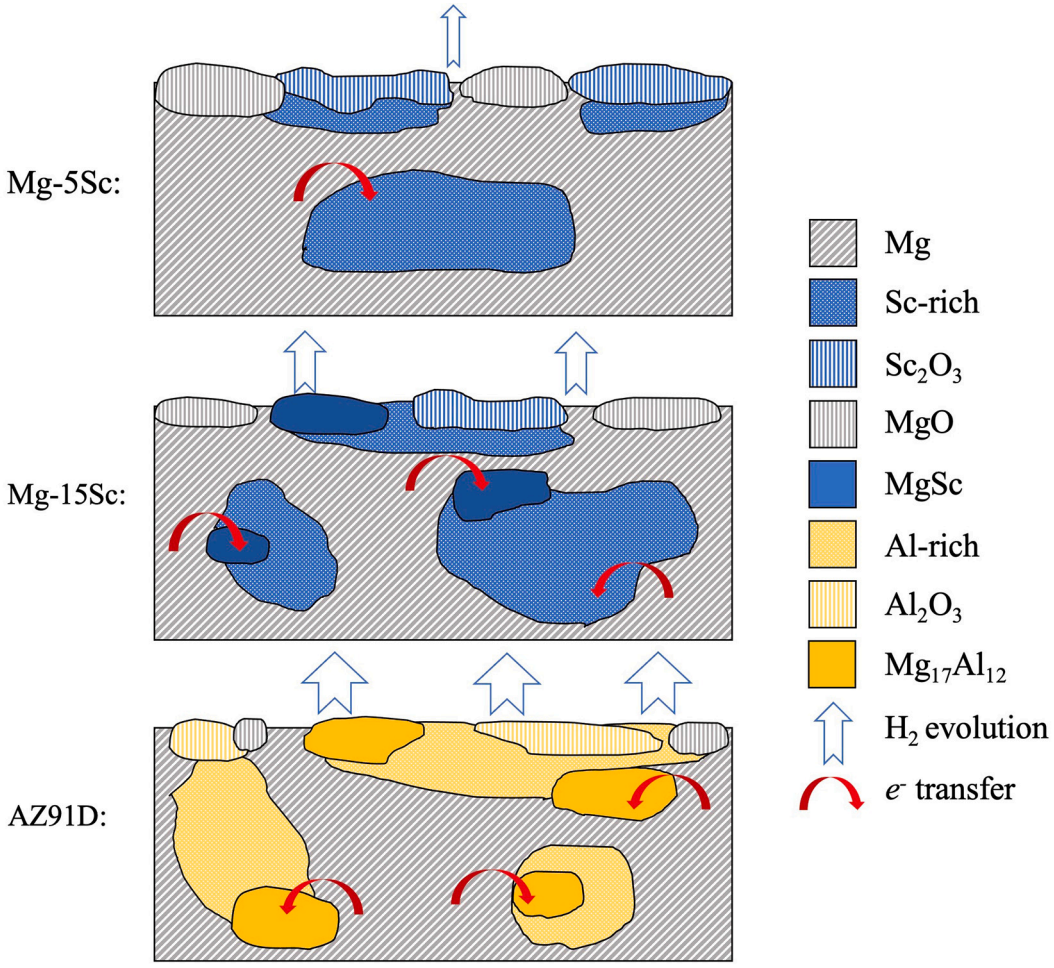

Fig. 14. Schematic diagram of the corrosion mechanism of Mg-*x*Sc and AZ91D alloys.

(2) The mechanical property is improved with the precipitation of MgSc phase, and the mechanical property of Mg-15Sc is comparable to that of AZ91D.
(3) According to the first-principles calculation and SKPFM experimental results, Mg-5Sc has the lowest potential difference, i.e., smallest corrosion tendency, whereas the MgSc phase leads to a large potential difference in binary-phase Mg-15Sc alloy.
(4) The surface of single-phase Mg-5Sc is relatively more protective than that of binary-phase Mg-15Sc and AZ91D. This may due to the absence of micro-galvanic corrosion induced by second phases, and the improvement of surface protection with the presence of the Sc_2O_3 in the surface layer.
(5) Although second phases are both present on the surface of Mg-15Sc and AZ91D alloys, the MgSc phase has a stronger ability to suppress cathodic reaction than that of $Mg_{17}Al_{12}$ phase, as the energy barrier for H_2O dissociation and H_2 combination is much bigger.

Data availability

The raw/processed data required to reproduce these findings cannot be shared at this time as the data also forms part of an ongoing study.

Declaration of Competing Interest

The authors declared that they have no conflicts of interest to this work. We declare that we do not have any commercial or associative interest that represents a conflict of interest in connection with the work submitted.

Acknowledgements

This work was supported by Shanghai Science and Technology Committee (No. 18511109300), Science and Technology Commission of the CMC (2019JCJQZD27300), Foundation from Shanghai Jiao Tong University (AF0500132, AF0500149), Funding from Center of Hydrogen Science of Shanghai Jiao Tong University. Thanks for the technology support from Instrumental Analysis Center, Shanghai Jiao Tong University.

Appendix A. Supplementary data

Supplementary data to this article can be found online at https://doi.org/10.1016/j.matchar.2021.111294.

References

[1] T. Ying, H. Chi, M. Zheng, Z. Li, C. Uher, Low-temperature electrical resistivity and thermal conductivity of binary magnesium alloys, Acta Mater. 80 (2014) 288–295, https://doi.org/10.1016/j.actamat.2014.07.063.
[2] G.L. Song, A. Atrens, Understanding magnesium corrosion-a framework for improved alloy performance, Adv. Eng. Mater. 5 (2003) 837–858, https://doi.org/10.1002/adem.200310405.
[3] A. Atrens, G.L. Song, F. Cao, Z. Shi, P.K. Bowen, Advances in Mg corrosion and research suggestions, J. Magnes. Alloys 1 (2013) 177–200, https://doi.org/10.1016/j.jma.2013.09.003.
[4] G.L. Song, A. Atrens, Corrosion mechanisms of magnesium alloys, Adv. Eng. Mater. 1 (1999) 11–33, https://doi.org/10.1002/(SICI)1527-2648(199909)1:1<11::AID-ADEM11>3.0.CO;2-N.
[5] R.W. Revie, H.H. Uhlig, Corrosion and Corrosion Control: An Introduction to Corrosion Science and Engineering, A John Wiley & Sons, INC., New Jersey, 2008, https://doi.org/10.1002/9780470277270.ch5.
[6] N.T. Kirkland, J. Lespagnol, N. Birbilis, M.P. Staiger, A survey of bio-corrosion rates of magnesium alloys, Corros. Sci. 52 (2010) 287–291, https://doi.org/10.1016/j.corsci.2009.09.033.
[7] K. Gusieva, C.H.J. Davies, J.R. Scully, N. Birbilis, Corrosion of magnesium alloys: the role of alloying, Int. Mater. Rev. 60 (2014) 169–194, https://doi.org/10.1179/1743280414y.0000000046.
[8] N. Birbilis, G. Williams, K. Gusieva, A. Samaniego, M.A. Gibson, H.N. McMurray, Poisoning the corrosion of magnesium, Electrochem. Commun. 34 (2013) 295–298, https://doi.org/10.1016/j.elecom.2013.07.021.
[9] R.L. Liu, J.R. Scully, G. Williams, N. Birbilis, Reducing the corrosion rate of magnesium via microalloying additions of group 14 and 15 elements, Electrochim. Acta 260 (2018) 184–195, https://doi.org/10.1016/j.electacta.2017.11.062.
[10] M. Deng, L. Wang, D. Höche, S.V. Lamaka, C. Wang, D. Snihirova, Y. Jin, Y. Zhang, M.L. Zheludkevich, Approaching "stainless magnesium" by Ca micro-alloying, Mater. Horiz. 8 (2021) 589–596, https://doi.org/10.1039/d0mh01380c.
[11] W. Xu, N. Birbilis, G. Sha, Y. Wang, J.E. Daniels, Y. Xiao, M. Ferry, A high-specific-strength and corrosion-resistant magnesium alloy, Nat. Mater. 14 (2015) 1229–1235, https://doi.org/10.1038/nmat4435.
[12] A. Boby, A. Srinivasan, U.T.S. Pillai, B.C. Pai, Mechanical characterization and corrosion behavior of newly designed Sn and Y added AZ91 alloy, Mater. Des. 88 (2015) 871–879, https://doi.org/10.1016/j.matdes.2015.09.010.
[13] A. Hiba, H. Abdelkader, D. Achour, R. Lyacine, S. Nico, D. Milan, B. François, H. Anne-Laure, B. Thierry, Impact of rare-earth elements on the corrosion performance of binary magnesium alloys, J. Alloys Compd. 829 (2020) 154569, https://doi.org/10.1016/j.jallcom.2020.154569.
[14] J. Meng, W. Sun, Z. Tian, X. Qiu, D. Zhang, Corrosion performance of magnesium (MMg) alloys containing rare-earth (RE) elements, in: Corrosion Prevention of Magnesium Alloys, Woodhead Publishing, Cambridge, 2013, https://doi.org/10.1533/9780857098962.1.38.
[15] Y. Huang, W. Gan, K.U. Kainer, N. Hort, Role of multi-microalloying by rare earth elements in ductilization of magnesium alloys, J. Magnes. Alloys 2 (2014) 1–7, https://doi.org/10.1016/j.jma.2014.01.005.
[16] J. Chang, X. Guo, S. He, P. Fu, L. Peng, W. Ding, Investigation of the corrosion for Mg-xGd-3Y-0.4Zr (x = 6, 8, 10, 12 wt%) alloys in a peak-aged condition, Corros. Sci. 50 (2008) 166–177, https://doi.org/10.1016/j.corsci.2007.06.003.
[17] K.R. Limmer, K.S. Williams, J.P. Labukas, J.W. Andzelm, First principles modeling of cathodic reaction thermodynamics in dilute magnesium alloys, Corrosion 73 (2017) 506–517, https://doi.org/10.5006/2274.
[18] C. Zhang, L. Wu, H. Liu, G. Huang, B. Jiang, A. Atrens, F. Pan, Microstructure and corrosion behavior of Mg-Sc binary alloys in 3.5 wt.% NaCl solution, Corros. Sci. 174 (2020) 108831, https://doi.org/10.1016/j.corsci.2020.108831.
[19] T. Zhang, X. Liu, Y. Shao, G. Meng, F. Wang, Electrochemical noise analysis on the pit corrosion susceptibility of Mg-10Gd-2Y-0.5Zr, AZ91D alloy and pure magnesium using stochastic model, Corros. Sci. 50 (2008) 3500–3507, https://doi.org/10.1016/j.corsci.2008.09.033.
[20] G. Kresse, J. Hafner, Ab initio molecular dynamics for liquid metals, Phys. Rev. B 47 (1993) 558–561, https://doi.org/10.1103/physrevb.47.558.
[21] J.P. Perdew, K. Burke, M. Ernzerhof, Generalized gradient approximation made simple, Phys. Rev. Lett. 50 (1996) 308–310, https://doi.org/10.1103/PhysRevLett.77.3865.
[22] P.E. Blöchl, Projector augmented-wave method, Phys. Rev. B 50 (1994) 17953–17979, https://doi.org/10.1103/physrevb.50.17953.
[23] Z. Luo, H. Zhu, T. Ying, D. Li, X. Zeng, First principles calculations on the influence of solute elements and chlorine adsorption on the anodic corrosion behavior of Mg (0001) surface, Surf. Sci. 672-673 (2018) 68–74, https://doi.org/10.1016/j.susc.2018.02.002.
[24] Z. Luo, J. Xu, Y. Wang, T. Xie, H. Zhu, T. Ying, D. Li, L. Wang, X. Zeng, C. Wolverton, W. Ding, Theoretical analysis of the galvanic corrosion behavior of Mg-Ge binary alloy, J. Electrochem. Soc. 166 (2019) C421–C427, https://doi.org/10.1149/2.1061913jes.
[25] A.A. Nayeb-Hashemi, J.B. Clark, The Mg-Sc (Magnesium-Scandium) system, Bull. Alloy Phase Diagr. 7 (1986) 574–578, https://doi.org/10.1007/BF02869876.
[26] H. Okamoto, Mg-Sc (Magnesium-Scandium), J. Phase Equilib. Diffus. 30 (2009) 660–661, https://doi.org/10.1007/s11669-009-9603-1.
[27] S.J. Yao, D.Q. Yi, S. Yang, X.H. Cang, W.X. Li, Effect of Sc on microstructures and corrosion properties of AZ91, Mater. Sci. Forum 546-549 (2007) 139–142, https://doi.org/10.4028/www.scientific.net/MSF.546-549.139.
[28] V.A. Shalomeev, N.A. Lysenko, E.I. Tsivirko, V.V. Lukinov, V.V. Klochikhin, Structure and properties of magnesium alloys with scandium, Met. Sci. Heat Tr. 50 (2008) 34–37, https://doi.org/10.1007/s11041-008-9006-7.
[29] O. Yukiko, A. Daisuke, S. Yuji, K. Junichi, A lightweight shape-memory magnesium alloy, Science 353 (2016) 368–370, https://doi.org/10.1126/science.aaf6524.
[30] D. Ando, Y. Ogawa, T. Suzuki, Y. Sutou, J. Koike, Age-hardening effect by phase transformation of high Sc containing Mg alloy, Mater. Lett. 161 (2015) 5–8, https://doi.org/10.1016/j.matlet.2015.06.057.
[31] Q. Peng, N. Ma, X. Li, J. Zhang, Age hardening response of a Mg-5wt.%Sc alloy under an applied stress field, Mater. Lett. 78 (2012) 58–61, https://doi.org/10.1016/j.matlet.2012.03.063.
[32] X. Liu, T. Zhang, Y. Shao, G. Meng, F. Wang, Effect of alternating voltage treatment on the microstructure and corrosion resistance of stannate conversion coating on AZ91D alloy, Corros. Sci. 51 (2009) 2685–2693, https://doi.org/10.1016/j.corsci.2009.07.009.
[33] P. Zhao, T. Xie, X. Xu, H. Zhu, F. Cao, T. Ying, X. Zeng, Designing high corrosion resistant peritectic magnesium alloys via Sc and Y addition, Metall. Mater. Trans. A 51 (2020) 2509–2522, https://doi.org/10.1007/s11661-020-05693-5.
[34] K. Huang, R. Han, Solid State Physics, Higher Education Press, Beijing, 1988.
[35] H. Ma, X.Q. Chen, R. Li, S. Wang, J. Dong, W. Ke, First-principles modeling of anisotropic anodic dissolution of metals and alloys in corrosive environments, Acta Mater. 130 (2017) 137–146, https://doi.org/10.1016/j.actamat.2017.03.027.
[36] L. Min, J. Ying, P. Jinshan, L. Christofer, Co-adsorption of H_2O, OH, and Cl on aluminum and intermetallic surfaces and its effects on the work function studied by DFT calculations, Molecules 24 (2019) 4284, https://doi.org/10.3390/molecules24234284.
[37] M. Santamaria, F. Di Quarto, S. Zanna, P. Marcus, Initial surface film on magnesium metal: a characterization by X-ray photoelectron spectroscopy (XPS)

and photocurrent spectroscopy (PCS), Electrochim. Acta 53 (2007) 1314–1324, https://doi.org/10.1016/j.electacta.2007.03.019.
[38] Y. Inoue, I. Yasumori, Catalysis by alkaline earth metal oxides. III. X-ray photoelectron spectroscopic study of catalytically active MgO, CaO, and BaO surfaces, Bull. Chem. Soc. Jpn. 54 (1981) 1505–1510, https://doi.org/10.1246/bcsj.54.1505.
[39] R. Hoogewijs, L. Fiermans, J. Vennik, Electronic relaxation processes in the KLL′ auger spectra of the free magnesium atom, solid magnesium and MgO, J. Electron Spectrosc. Relat. Phenom. 11 (1977) 171–183, https://doi.org/10.1016/0368-2048(77)85108-6.
[40] C.H. Xu, C. Wei, Pilling-Bedworth ratio for oxidation of alloys, Mater. Res. Innov. 3 (2000) 231–235, https://doi.org/10.1007/s100190050008.
[41] Z.N. Ma, X. Wang, T.T. Yan, Q. Li, Q.C. Xu, J.L. Tian, L. Wang, First-principles study on thermodynamic stability and electronic characteristics of long-period stacking ordered phases in Mg-Zn-Y alloys, J. Alloys Compd. 708 (2017) 29–33, https://doi.org/10.1016/j.jallcom.2017.02.172.
[42] J.A. Yuwono, C.D. Taylor, G.S. Frankel, N. Birbilis, S. Fajardo, Understanding the enhanced rates of hydrogen evolution on dissolving magnesium, Electrochem. Commun. 104 (2019) 106482, https://doi.org/10.1016/j.elecom.2019.106482.
[43] S. Ganeshan, S.L. Shang, H. Zhang, Y. Wang, M. Mantina, Z.K. Liu, Elastic constants of binary Mg compounds from first-principles calculations, Intermetallics 17 (2009) 313–318, https://doi.org/10.1016/j.intermet.2008.11.005.
[44] K. Chen, K.P. Boyle, Alloy solid solution strengthening of Mg alloys: valence effect, Phys. Status Solidi B 249 (2012) 2089–2095, https://doi.org/10.1002/pssb.201248195.